

Noterdaeme et al. 2012). As such, DLAs are keys to understanding galaxy formation and evolution since they are thought to be the reservoir of atomic gas for stellar formation in galaxies. They are thus an important probe of physical conditions in the interstellar medium at high redshifts (Petitjean et al. 2000; Fumagalli et al. 2013; Bird et al. 2014; Ota et al. 2014; Fumagalli et al. 2016; Rudie et al. 2017).

But DLAs are also contaminants in the measurements of the Lyman- α ($\text{Ly}\alpha$) forest flux probability distribution function (Lee et al. 2015), its 3D auto-correlation function (Slosar et al. 2011; Bautista et al. 2017; du Mas des Bourboux et al. 2020) or its 1D power spectrum (McDonald et al. 2006; Palanque-Delabrouille et al. 2013; Chabanier et al. 2019). Since DLAs form at high density peaks they cluster more strongly than diffuse $\text{Ly}\alpha$ clouds (Font-Ribera & Miralda-Escudé 2012), thus biasing astrophysical and cosmological parameters if not well accounted for. Therefore, their detection along with the measurements of their physical properties, absorption redshift and column densities, are important in such studies.

With hundreds of thousands detected quasar spectra, the large statistical power of the Sloan Digital Sky Survey (SDSS, York et al. (2000)) has fostered the compilation of DLA catalogs (Noterdaeme et al. 2009; Prochaska & Wolfe 2009; Zhu & Ménard 2013; Garnett et al. 2017; Parks et al. 2018; Ho et al. 2020). Given the tremendous number of spectra to analyze, it has also played a critical role for the development of automated detection algorithms over visual inspection, e.g. using Voigt-profile fitting (Prochaska et al. 2005; Noterdaeme et al. 2009, 2012) or machine learning techniques such as convolutional neural networks (CNN, Parks et al. (2018)), Gaussian processes (Garnett et al. 2017) or random forest classifiers (Fumagalli et al. 2020).

The final SDSS-IV quasar catalog from Data Release 16 (DR16) of the extended Baron Oscillation Spectroscopic Survey (eBOSS, Dawson et al. (2016); Ahumada et al. (2020)), which we will refer to as DR16Q, is the largest quasar spectra sample to date with 920,110 observations of 750,414 quasars (Lyke et al. 2020). In the DR16Q, we used the CNN algorithm from Parks et al. (2018) to include DLA quasar identification for very confident DLAs with $\log N(H_I) \geq 20.3$ only. Here we present the full sample of absorbing systems detected with the CNN in DR16Q, which includes less confident DLAs and Lyman Limit Systems (LLS) with $\log(N(H_I))$ as low as 19.7. The choice of the CNN from Parks et al. (2018) is motivated by the design of the algorithm constructed specifically for low redshift and low signal to noise BOSS/eBOSS quasar spectra.

The paper is organized as follow. Sec. 2 presents the quasar spectra sample which is scanned for high column density absorbing systems. Sec. 3 introduces the automated algorithm and the CNN architecture from Parks et al. (2018) that we use to detect strong absorbers. We perform efficiency and purity validation of the algorithm with synthetic spectra and a study of biases of DLA parameters, $\log(N(H_I))$ and z_{DLA} in Sec. 4. Finally, we present the full absorber sample in Sec. 5 and compare it with existing catalogs. We present concluding remarks in Sec. 6.

2. QUASAR SPECTRA SAMPLE DR16Q

In this work, we use data measured with BOSS and eBOSS (Dawson et al. 2016) of the SDSS-III and SDSS-IV (Gunn et al. 2006; Smee et al. 2013; Blanton et al. 2017) surveys respectively. We focus on the $\text{Ly}\alpha$ forest regions from the 750,414 quasar spectra available in DR16Q (Lyke et al. 2020), which contains all SDSS spectroscopically observed quasars. The selection of quasars for the BOSS and eBOSS surveys are described in Ross et al. (2012); Myers et al. (2015).

We search for DLAs in the 263,201 spectra with $2 \leq Z_{\text{LYAWG}} \leq 6$, the redshift range over which spectra contain enough pixels to identify DLAs. We use the quasar redshift estimator, Z_{LYAWG} , generated by Principal Component Analysis (PCA), using the REDVSBUE algorithm¹. The DR16Q catalog is constructed from the SPALL-v5_13_0 (spAll) file containing all SDSS-III/IV observations treated by the version v5_13_0 of the SDSS spectroscopic pipeline². If multiple observations are available for one object in the spAll file, we use the stacked spectrum of all good observations as input to the DLA finder. We identify bad spectra using the ZWARNING parameter. If ZWARNING was SKY, LITTLE COVERAGE, UNPLUGGED, BAD TARGET, or NODATA, we did not use the associated observation in the stack.

Fig. 1 shows the redshift distribution of the forest pixels, with a mean of $z = 2.4$. Fig. 2 shows the flux and signal-to-noise (S/N) averaged over the forest, with a mean of $2.87 \times 10^{-19} \text{ W m}^{-2} \text{ nm}^{-1}$ and 2.90, respectively. We will see in Sect. 4.2 that the efficiency for finding DLAs is poor for forests with low S/N corresponding generally to forests with low fluxes. Fig. 2 therefore also shows the S/N for a “bright sample” of forests with mean forest flux $\overline{f_\lambda} > 2 \times 10^{-19} \text{ W m}^{-2} \text{ nm}^{-1}$. Also shown is the S/N as a function of $\overline{f_\lambda}$ for three redshift ranges. We

¹ <https://github.com/londumas/redvsblue>

² https://data.sdss.org/datamodel/files/BOSS_SPECTRO_REDUX/RUN2D/spAll.html

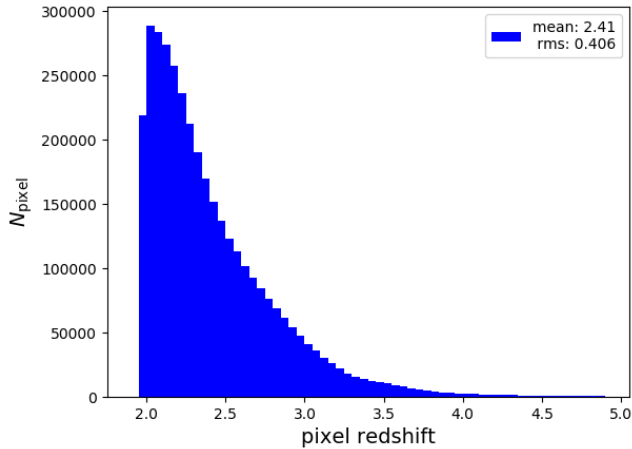


Figure 1. Redshift distribution for pixels in the Ly α forest from quasar spectra available in DR16Q.

see that bright forests generally have S/N greater than 2.

3. DLA DETECTION METHOD

We identified DLAs with the algorithm described in Parks et al. (2018), which is based on a multi-task learning CNN. We refer the reader to Parks et al. (2018) for a complete description of the detection algorithm, only recalling here the major steps. The CNN architecture and its training aim at constructing an algorithm that works at low redshifts, in noisy regions, and without any input from the user other than raw spectral data. The algorithm therefore does not need quasar continuum or DLA Voigt profile modeling and it ignores flux errors estimated by the SDSS pipeline. Finally, the model does not include Broad Absorption Lines (BALs), compromising DLA detection. Therefore we reject lines of sight that the DR16Q pipeline indicates as affected by BALs.

The neural network model uses a standard 2D CNN architecture with four layers. It relies on the Adam (Adaptive Moment Estimation) algorithm to search for the optimal parameters (Kingma & Ba 2014) and is implemented using the Google’s deep learning framework TensorFlow³. It analyzes 1,748-pixel long sightlines of $\delta\lambda \simeq 1 \text{ \AA}$ in 1,748 inference steps with 400-pixel long sliding windows in the $900 \text{ \AA} \leq \lambda \leq 1,346 \text{ \AA}$ region in order to improve detection of multiple DLAs per-sightline. The 400-pixel size is in part imposed by the SDSS resolution. The model produces three outputs for each sliding window: (1) classification of the segment as containing a DLA or not, (2) the DLA absorption red-

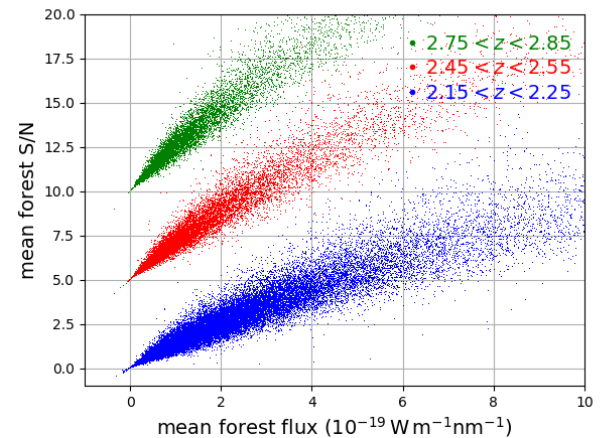
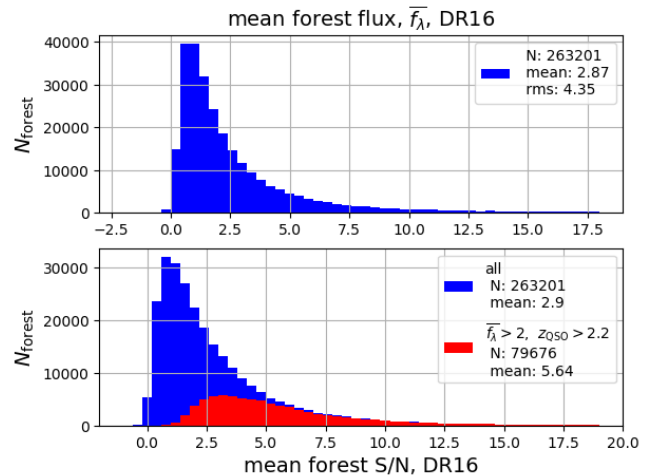


Figure 2. The mean flux and mean signal-to noise ratio (S/N) for pixels in the Ly α forest. **Top panel:** shows the distribution for the complete sample (blue) and for the restricted sample with high DLA detection efficiency: quasar redshift $z_{\text{QSO}} > 2.2$ and mean forest flux $\bar{f}_\lambda > 2.0$. **Bottom panel:** shows S/N as a function of \bar{f}_λ for three ranges of mean forest redshift as labeled. For clarity the S/N is offset by (0,5,10) units.

shift Z_{DLA} , i.e. the pixel center localization and (3) the HI column density, NHI_{DLA} , if a DLA is visible. In the case of a detected DLA in a sightline, the authors also define a non statistical measure of confidence, the *confidence* parameter over the range (0,1). It is based on how robustly the DLA is localized over the different predictions of the sliding window.

The training sample was constructed using 4,113 SDSS sightlines, with quasar redshift $z_{\text{QSO}} > 2.3$ and signal to noise $\text{S/N} > 5$, identified as DLA-free from the analysis of Prochaska & Wolfe (2009). The authors generated 200,000 sightlines from the DLA-free sample by inserting DLAs and super Lyman-limit systems (SLLS)

³ <https://www.tensorflow.org/>

with logarithmic column density $19.5 \leq \log N(H_I) \leq 22.5$ using Voigt profile modeling.

Finally, the algorithm was validated using one catalog with synthetic DLA in real DLA-free spectra and one catalog constituted of visually inspected spectra containing DLAs (Prochaska & Wolfe 2009). The authors found a systematic bias of order ~ 0.1 in the predicted $\log N(H_I)$ at both low and high ends. They fit this bias with a 3^{rd} degree polynomial (see Fig.9 of Parks et al. (2018)) and used this result to correct for the bias in the final automated algorithm.

4. ANALYSIS OF DLAS IN MOCK SPECTRA

Given that S/N and quasar redshift distributions of the training and validation samples do not exactly match those of DR16 data, we used synthetic spectra to perform purity and efficiency validation of the algorithm along with an investigation of systematics on the inferred z_{DLA} and $N(H_I)$. The synthetic spectra, hereafter “mocks”, were produced for the eBOSS Ly α data analysis (du Mas des Bourboux et al. 2020). In Sec. 4.1 we briefly describe the construction of mock spectra and we present our estimates of efficiency and purity in Sec. 4.2. The accuracy and precision of the estimation of $N(H_I)$ is discussed in Sec. 4.3.

4.1. Synthetic quasar spectra

The production of the mocks is described elsewhere (Etourneau et al. 2021), and we describe here only the major steps. A low resolution Gaussian random density field was produced in a box of $2560 \times 2560 \times 1536$ voxels of $2.19 h^{-1}$ Mpc sides. Quasar positions were drawn proportionally to a lognormal field, with phases in Fourier space equal to those of the density field. The interpolated values of the density field along the sightlines from the observer position towards the quasars were computed, together with the 3 components of the velocity and the 6 components of the velocity gradient tensor. Extra small-scale fluctuations were added to each sightline independently, in order to reproduce the variance in the Ly α forest in the data. Redshift space distortions were implemented by adding the velocity gradient along the sightlines to the density field. We then applied a log-normal transformation to this sum, and used the Fluctuating Gunn-Peterson Approximation (FGPA) to compute the optical depth in each cell.

We define high column density systems (HCD) as systems with column density, $N(H_I) > 10^{17.2}$, including both DLA and Lyman limit systems $10^{17.2} < N(H_I) < 2 \times 10^{20}$. We selected peaks of the large-scale density field as possible locations of HCD and set the threshold to get a constant bias $b_{\text{HCD}}(z) = 2$ for the HCD, us-

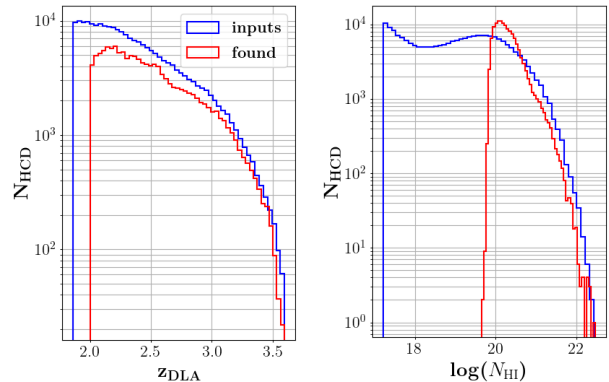


Figure 3. Mock HCD distribution of z_{DLA} (left) and $\log N(H_I)$ (right) as placed in mocks (blue) and recovered by the CNN (red). Mock spectra have a total of 218,124 HCDs. Among them, 91,659 HCDs have $\log N(H_I) \geq 19$ and $z_{\text{DLA}} \geq 2$. The CNN detects 132,226 absorbing systems with $\log N(H_I) \geq 19.6$ and $z_{\text{QSO}} > z_{\text{DLA}} \geq 2$. The CNN has not been trained for absorbers with $\log N(H_I) < 19.5$ but it still detects HCDs with $\log N(H_I)$ slightly below this threshold value, which explains the excess at the low end of the $\log N(H_I)$ distribution for the CNN.

ing formulas in appendix A of (Font-Ribera & Miralda-Escudé 2012). We then Poisson sampled the selected peaks to follow the HCD redshift distribution of the default model from the IGM physics package pyigm⁴. The column density was selected to follow the same model. These distributions are illustrated in Fig. 3. The radial velocity of the HCD was obtained from the three velocity-component boxes. This information was included in a HCD catalog.

In a last step, the quasar spectra are produced by multiplying the transmitted flux fraction by a quasar continuum and adding instrumental noise (Gonzales-Morales et al. (in preparation)). For each HCD in the catalog, we multiplied the corresponding quasar spectrum by the Voigt profile for the HCD column density.

Figure 4 shows the mean flux and mean S/N for mock pixels in the Ly α forest. We see that the mock distribution agree qualitatively with the data, shown in Fig. 2. The data do, however, contain more forests with very low flux and very high flux.

4.2. Efficiency and purity

The efficiency for DLA-detection and the purity of the detected sample were studied by using the mock spectra where the catalog of detected DLAs can be compared with the catalog of generated HCDs. The model reports a total of 132,226 candidate absorbing systems

⁴ <https://github.com/pyigm/pyigm>

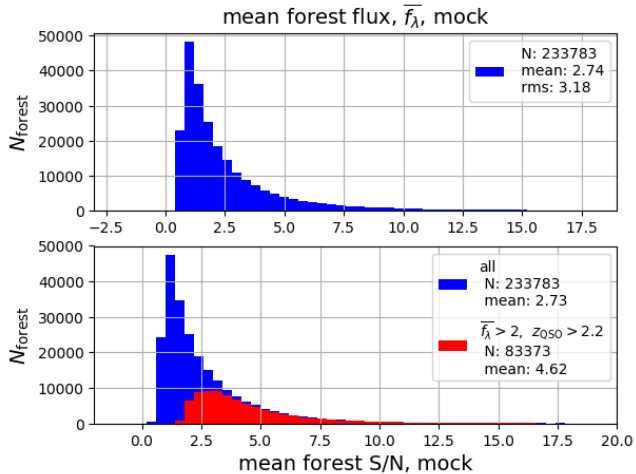


Figure 4. Mean flux and mean S/N for mocks pixels in the Ly α -forest for the complete sample (blue) and for the restricted sample with high DLA detection efficiency (red): quasar redshift $z_{\text{QSO}} > 2.2$ and mean forest flux $\bar{f}_\lambda > 2.0$.

with $z_{\text{DLA}} < z_{\text{QSO}}$ and $z_{\text{DLA}} \geq 2$ in 92,042 sightlines with $\log N(H_I)$ and z_{DLA} distributions shown in Fig 3.

Both efficiency and purity are functions of the characteristics of the forest (signal-to-noise ratio and forest mean flux) and of the DLA (redshift and column density). They also depend on the criterion used to define detected DLAs, i.e. the requirements placed on the confidence parameter and on the required agreement between generated and found z_{DLA} and $N(H_I)$.

The criterion for detection and matching are arbitrary to a certain extent. The most important matching criterion concerns the redshift difference between generated and detected DLAs. Fig. 5 shows this difference vs the mean forest flux, \bar{f}_λ for best matched DLAs, where the match only requires that mock and found DLAs are on the same sightline. Here, we adopt a matching criterion requiring that detected and generated redshifts differ at most by $\Delta z < 0.02$ (about 25Å). This redshift-matching cut accepts most detected DLAs for $\bar{f}_\lambda > 2 \times 10^{-19} \text{ W m}^{-2} \text{ nm}^{-1}$. However, the redshift resolution degrades substantially for lower \bar{f}_λ . With the above criterion, the DLA finder recovers 62,847 absorbing systems with $z_{\text{DLA}} > 2$ and $\log N(H_I) > 19$ (69% of the absorbing systems put in mocks). Among them 86% (70%) have confidence parameters > 0.5 (> 0.9). Changing the redshift-matching criterion to $\Delta z < 0.01$ reduces only slightly the number of recovered DLAs from 63,847 to 61,131.

For the adopted matching criterion, $\Delta z_{\text{DLA}} < 0.02$, the efficiency and purity as a function of z_{DLA} and $N(H_I)$ are shown in Fig. 6 on the left and right panels respectively. Fig. 7 and Fig. 8 show the same measure-

ments but for bright ($\bar{f}_\lambda > 2 \times 10^{-19} \text{ W m}^{-2} \text{ nm}^{-1}$) and faint ($\bar{f}_\lambda > 2 \times 10^{-19} \text{ W m}^{-2} \text{ nm}^{-1}$) forests respectively. Note that we use HCD characteristics as returned by the finder to compute the purity and the ones from the mock input for the efficiency, which explains why the right panel does not have data for $\log N(H_I) < 19.65$ but the left one does.

For the bright sample, Fig. 7 shows that high efficiency (> 0.9) and purity (> 0.9) is obtained for column densities in the range $20.2 < \log N(H_I) < 22.0$ and redshifts $z_{\text{DLA}} > 2.2$. For the faint sample, high efficiency and purity is found only for $\log N(H_I) > 21.0$ and $z_{\text{DLA}} > 2.2$.

For the efficiency, there is almost no dependence with z_{DLA} . It is degraded for $z_{\text{DLA}} \leq 2.2$ but performs quite equally for higher redshifts. The bad performances at low absorbing redshifts happen since they occur in the blue and noisy end of the spectra (see S/N distribution as a function of quasar redshift in the bottom panel of Fig 2). Indeed, false negatives have a mean forest flux 25% lower than the average. By comparing Figs. 6, 7, and 8 we easily deduce that faint forests are driving the bad performances. Also, because the spectra is small in size at low redshifts, i.e. with a low number of pixels, it is harder for the CNN to detect features and to do accurate predictions. The efficiency drops below 0.2 for the low-end of $N(H_I)$, for which the CNN has not been specifically designed and trained and for which instrumental noise and resolution make detection difficult. The finder detects HCDs with $\log N(H_I)$ as low as 19 but, as we will see in the next section, overestimates this parameter. This explains the excess of the detected $\log N(H_I)$ near the detection threshold compared to the mock distribution on the left panel of Fig. 3

The efficiency also decreases for high $N(H_I)$ where the DLA covers a substantial fraction of the forest. While we observe a trend for a decrease toward the high-end of $N(H_I)$, synthetic spectra have a total of 806 HCD with $\log N(H_I) > 21.5$. While this makes our results statistically significant for high- $N(H_I)$ on average, results can be very noisy when sampled into z_{DLA} bins. Over the 104 missed DLAs with $\log N(H_I) > 21.5$ and $z_{\text{DLA}} > 2.2$, 19 are detected by the finder but rejected by the redshift-matching cut criterion ($0.02 < \Delta z < 0.04$) because of low mean forest flux ($\bar{f}_\lambda < 2$). Four have an absorbing redshift extremely close to the Ly α emission line such that the CNN found a $z_{\text{DLA}} > z_{\text{QSO}}$, 15 are part of two overlapping DLAs with $\Delta z_{\text{DLA}} < 0.03$ detected as one DLA with a higher $N(H_I)$ (as was noted in Parks et al. (2018), the CNN struggles at identifying overlapping DLAs). The 66 remaining have particularly low mean forest fluxes with an average of $\sim 0.3 \times 10^{-19} \text{ W m}^{-2} \text{ nm}^{-1}$. When considering bright

forests only, with $\bar{f}_\lambda > 2 \times 10^{-19} \text{ W m}^{-2} \text{ nm}^{-1}$, the efficiency is always > 0.9 for $20 < \log N(H_I)$. The results are noisy for $\log N(H_I) > 21.5$, especially for high-redshift bins, but the efficiency is close to one on average for $\log N(H_I) > 21.5$ DLAs.

The purity is > 0.5 for $z_{\text{DLA}} < 3.2$ and $20.3 < \log N(H_I) < 21.5$, and > 0.9 for $z_{\text{DLA}} < 3.2$ and $20.8 < \log N(H_I) < 21.5$.

Our matching criterion does not use the confidence parameter and using it could increase the purity at the cost of decreasing efficiency. Fig. 9 shows the distribution of the confidence parameter for all found HCDs, true positives and false positives. False positives are all HCDs found by the CNN but that has not been matched to a HCD input (same sightline with $\Delta z_{\text{DLA}} < 0.02$.) Only 18% (44%) of false positives are *confident* HCDs with confidence parameter > 0.9 (> 0.5). Taking only HCDs with confidence parameter > 0.9 brings the purity to be always > 0.9 for $\log N(H_I) > 20.3$.

The net decrease of the purity toward low $\log N(H_I)$ seen in the right panel of Fig. 6 occurs since it gets more and more difficult for the CNN to distinguish between real but relatively small absorptions and noise. Indeed, when considering bright forests only (see right panel of Fig 7), with $\bar{f}_\lambda > 2 \times 10^{-19} \text{ W m}^{-2} \text{ nm}^{-1}$, the purity is always > 0.9 for $20.1 < \log N(H_I)$. We observe a decrease of purity at high redshifts for both bright and faint samples (see Figs. 6,7,8) since the mean flux decreases for high redshift quasar making it harder for the CNN to distinguish between Ly α absorptions and DLAs.

To summarize, the main parameter for maximal completeness and purity of the absorber catalog is the mean flux of the forest. Taking $\bar{f}_\lambda > 2$ ensures efficiency and purity to be > 0.9 for $\log N(H_I) > 20.1$. However, it degrades the size of the sample. If taking all bright and faint forests, the efficiency is > 0.9 for $z_{\text{DLA}} > 2.2$ and $20 < \log N(H_I) < 21.5$, and purity is > 0.9 for $z_{\text{DLA}} < 3.2$ and $20.5 < \log N(H_I) < 21.5$ and confidence > 0.9 .

4.3. Parameter estimation

The CNN cannot be expected to give an unbiased estimate of $\log N(H_I)$ because the DLA sample was selected by the CNN. The mocks contain a large number of low column-density HCDs (Fig. 3) and some, through noise, may appear as detectable DLAs with $\log N(H_I) > 20$. As such, we expect that the estimated $\log N(H_I)$ to be on average greater than the true $\log N(H_I)$. This expectation is confirmed by Fig. 10 which compares the values of $N(H_I)$ returned by the finder with the input value from the mocks.

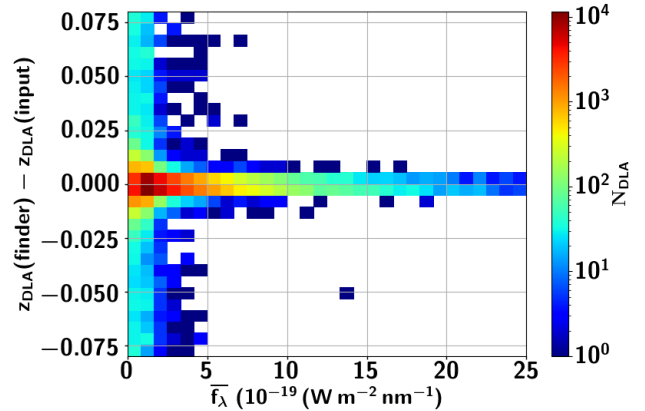


Figure 5. Mean difference between detected and generated DLA redshifts vs the mean forest flux, \bar{f}_λ .

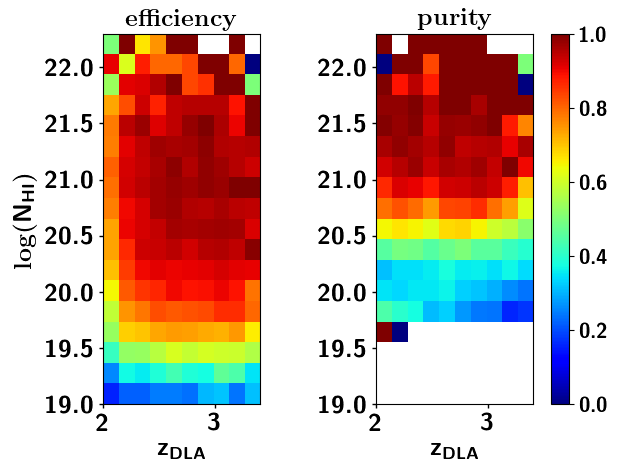


Figure 6. Efficiency (left) and purity (right) vs. redshift and column density using matching criterion $\Delta z_{\text{DLA}} < 0.02$.

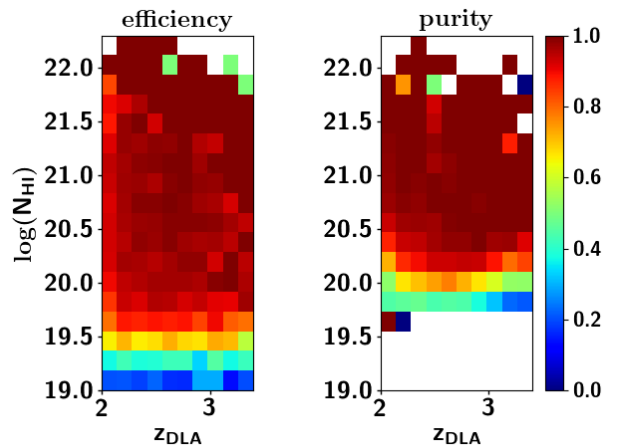


Figure 7. Same than for Fig. 6 for forests with $\bar{f}_\lambda > 2 \times 10^{-19} \text{ W m}^{-2} \text{ nm}^{-1}$.

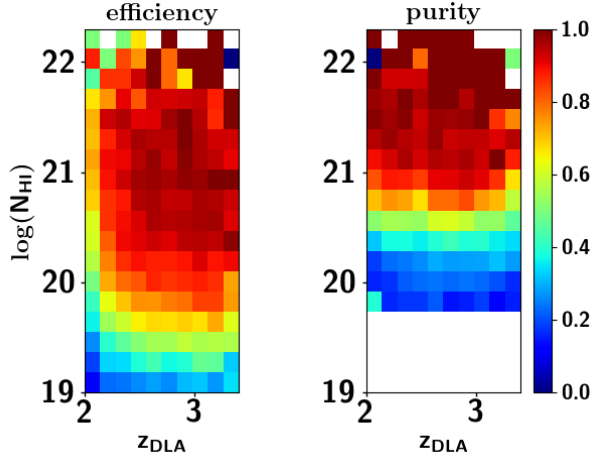


Figure 8. Same than for Fig. 6 for forests with $\bar{f}_\lambda < 2 \times 10^{-19} \text{ W m}^{-2} \text{ nm}^{-1}$.

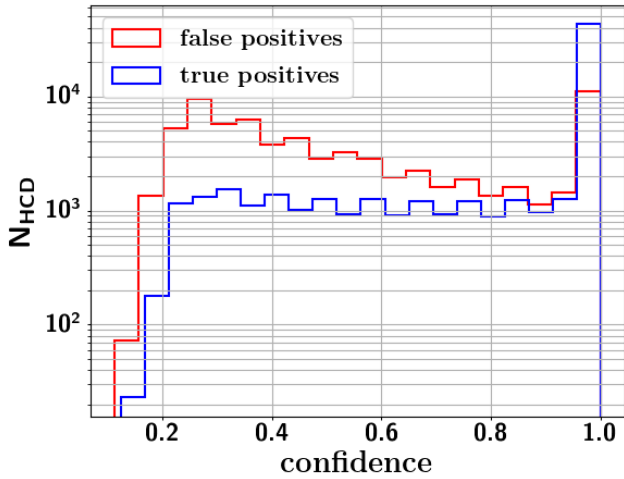


Figure 9. Confidence parameter distributions for the 132,226 absorbing systems found by the CNN: 69,380 false positives (red) and 62,846 true positives (blue). False positives are defined as HCDs found by the CNN but that do not matched HCD input. To match an input HCD, it must be on the same sightline with $\Delta z_{\text{DLA}} < 0.02$.

We investigate the dependence of this systematic bias on the confidence parameter in Fig. 11 showing the difference between input and CNN values of $\log N(H_I)$ for four ranges of CNN values of $\log N(H_I)$. First, as already seen in Fig. 10, it shows that the bias is worse for low $\log N(H_I)$ as the mean increases toward 0 when increasing $\log N(H_I)$. But more importantly, it demonstrates that the confidence parameter is a good indicator of biased $N(H_I)$ since the blue curves always tend toward more negative values than the red curves. The $\Delta \log N(H_I)$ tail of non-confident HCDs is particularly long on the top left panel. This is because even if these

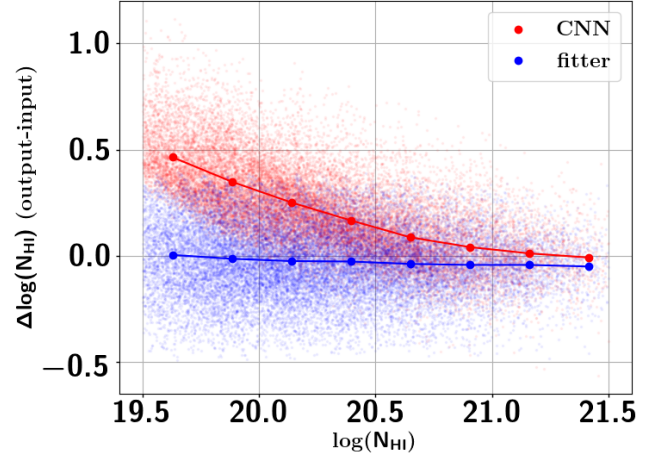


Figure 10. Difference in output and input values of $N(H_I)$ (in red for the CNN and blue for the fitter) vs input for the 21,234 found DLAs in the Ly α forest, i.e. in the rest-frame range $1,040\text{\AA} \leq \lambda_{\text{RF}} \leq 1,216\text{\AA}$.

low- $N(H_I)$ candidates are matched to input HCDs, we are close to the $N(H_I)$ detection threshold, so that many detected HCDs are in fact noise fluctuations close to a low- $N(H_I)$ HCD. As such, the confidence parameter is also very useful to increase the purity in the low- $N(H_I)$ regime.

To provide a more unbiased estimate of $\log N(H_I)$ we developed a DLA fitter and applied it to DLA candidates in the rest-frame range $1,040\text{\AA} \leq \lambda_{\text{RF}} \leq 1,216\text{\AA}$ and $\log N(H_I) < 22$. Fig. 10 shows the difference between the input $N(H_I)$ and Voigt-profile fitted $N(H_I)$, which are more accurate than the CNN ones.

5. THE DR16 DLA CATALOG

We applied the automated algorithm to the 263,201 DR16 quasar spectra sample described in Sec. 2. A total of 176,807 HCDs were found with $z_{\text{QSO}} > z_{\text{DLA}}$ and $z_{\text{DLA}} \geq 2$ in 112,155 sightlines. These numbers reduced to 117,458 absorbers in 78,018 sightlines when we reject BAL quasars with $\text{BAL_PROB} > 0$, among them 39,067 (33%) are classified as confident with confidence > 0.9 . Fig. 12 shows the z_{DLA} and $\log N(H_I)$ distributions for the 20,375 bright forests and the remaining 97,083 faint forests of the 117,458 total sample. The sample was further reduced to 57,136 absorbers with $\log N(H_I) \geq 20.3$ in 20,016 sightlines, yielding a purity of ~ 0.3 given that the number of DLAs per los should be roughly < 1 (Noterdaeme et al. 2012; Bird et al. 2014). Only considering bright forests raises the purity to be > 0.9 for DLAs with $\log N(H_I) \geq 20.3$ since the CNN found 6,996 such absorbers in 6,293 lines of sight.

The DLA sample we presented in DR16Q Lyke et al. (2020) only include DLAs absorbers with $\log N(H_I) \geq$

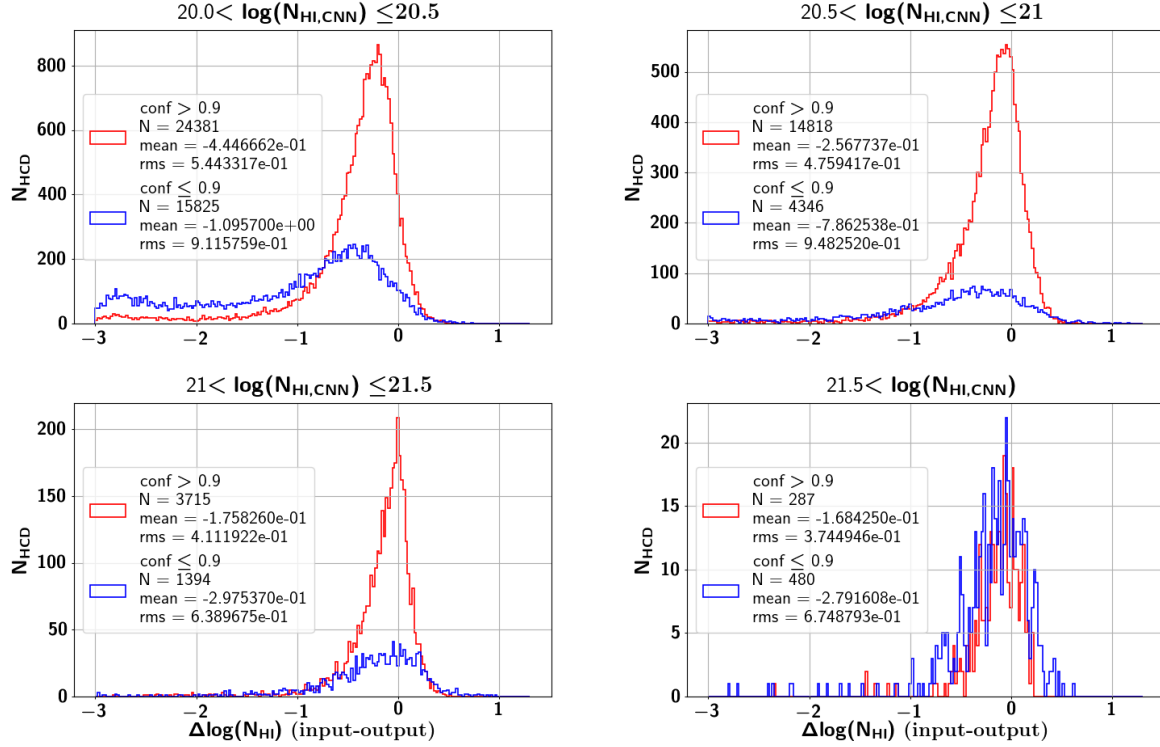


Figure 11. Distributions of the difference in $\log N(H_I)$ between the CNN predictions and the mock inputs for DLA candidates with confidence > 0.9 (red) and confidence ≤ 0.9 (blue). The distributions are shown in four ranges of $\log N(H_I)$ (CNN value) as labeled.

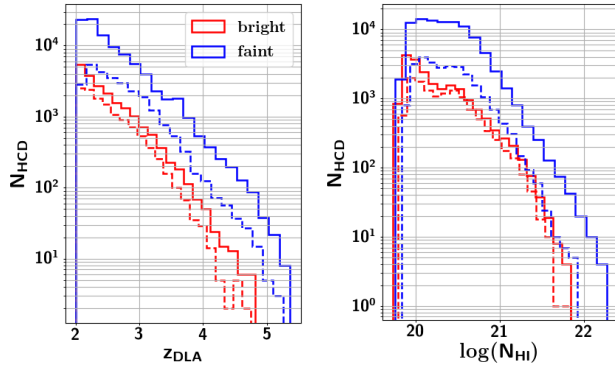


Figure 12. Distribution of z_{DLA} and $\log N(H_I)$ of the 117,458 absorbers detected by the CNN in DR16Q for the 20,375 bright forests with $\overline{f_\lambda} > 2 \times 10^{-19} \text{ W m}^{-2} \text{ nm}^{-1}$ (red) and the remaining 97,083 faint forests with $\overline{f_\lambda} \leq 2 \times 10^{-19} \text{ W m}^{-2} \text{ nm}^{-1}$ (blue). The dashed lines show the same samples reduced to confident absorbers only with confidence ≥ 0.9 .

20.3 and confidence > 0.9 and we did not reject BAL quasars. As presented in Sec. 4.2, the confidence cut highly degrades efficiency toward high $N(H_I)$ and low absorbing redshifts. The DLA sample presented here is consequently more complete and less pure. As discussed in Sect. 4.2, users of this catalog can construct their own selection criteria, depending on their specific needs.

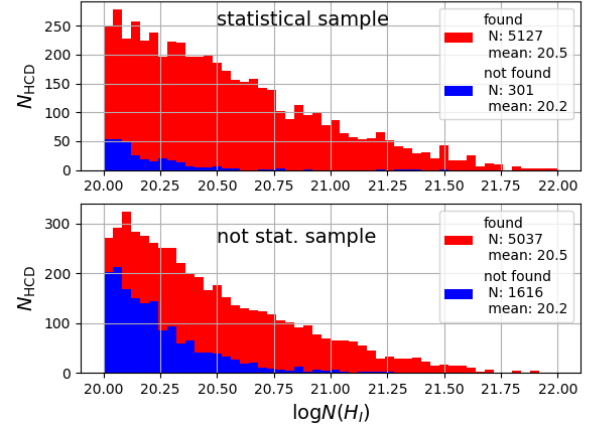


Figure 13. Distribution of $N(H_I)$ for the 12,081 DLAs of Noterdaeme et al. (2012) (N12) found and not found by the CNN in red and blue respectively. The statistical sample consists of confident DLA candidates with high signal to noise which are used in Noterdaeme et al. (2012) to measure the $\log N(H_I)$ distribution and the cosmological mass density of neutral gas.

We compared our sample of 117,458 absorbers with two other catalogs based on BOSS and eBOSS data. The first is the 12,081 absorber sample of Noterdaeme et al. (2012), hereafter N12, based on the DR9 SDSS

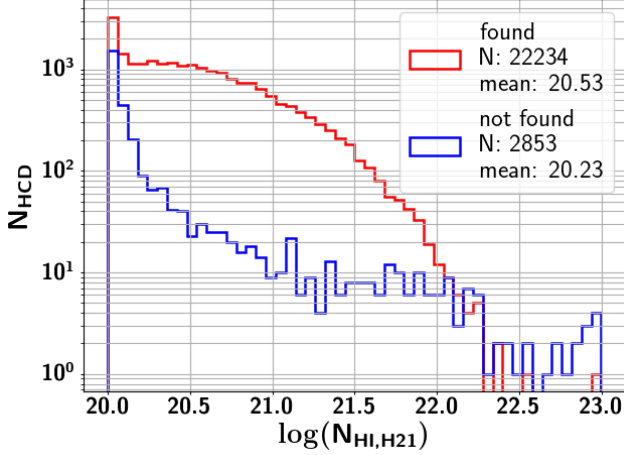


Figure 14. Distribution of $N(H_I)$ for the 25,087 confident DLAs ($p_{\text{DLA}} > 0.9$) of Ho et al. (2021) (H21) found and not found by the CNN in red and blue respectively.

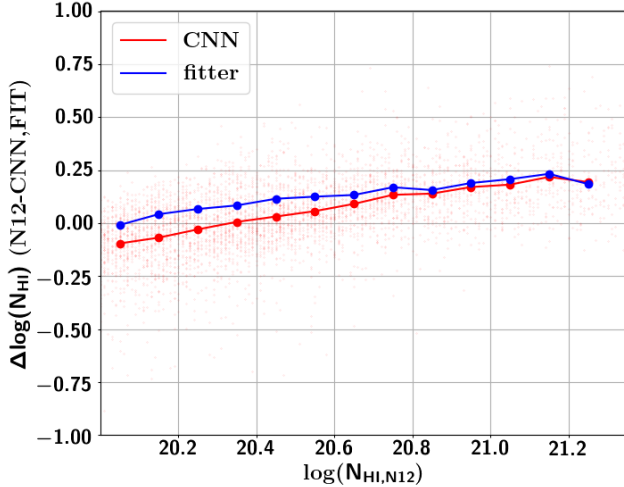


Figure 15. Comparison of the 4,620 $N(H_I)$ of the DR9 absorbers in the forest, i.e. in the rest-frame range $1,040\text{\AA} \leq \lambda_{\text{RF}} \leq 1,216\text{\AA}$, found in both N12 and this study, using either the CNN (red) or the fitter (blue) result.

data release that uses Voigt profile fitting procedure. The second, based on DR16 SDSS data, was provided by Ho et al. (2021), hereafter H21, that extends the Gaussian Processes method presented in Garnett et al. (2017). We reject BAL quasars with $\text{BAL_PROB} > 0$ and consider only DLA with a high probability, $p_{\text{DLA}} > 0.9$. With these criteria, their sample contains a total of 25,087 absorbers.

Given that the efficiency and purity of the catalogs are functions of cuts on signal-to-noise, mean forest flux, and the DLA parameters $\log N(H_I)$ and z_{DLA} , we do not expect perfect overlap between the catalogs. This fact is illustrated in Fig. 13 for N12. As for the mock

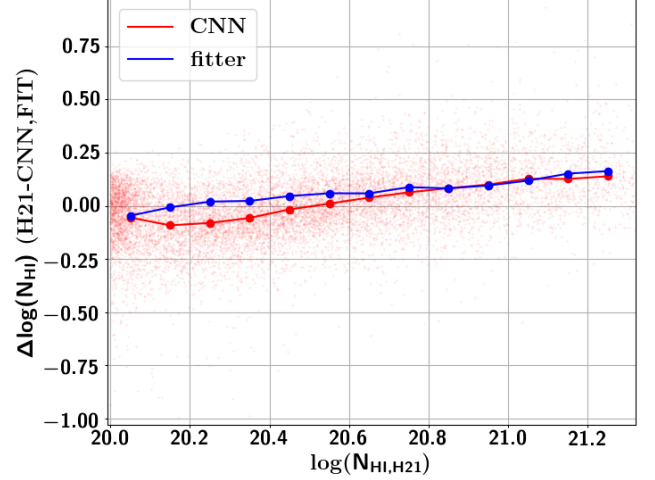


Figure 16. Same as Fig. 15 for H21. The sample contains 11,935 absorbers in the forest.

study in Sec. 4.2, DLAs are matched if they are in the same sightline and have absorbing redshifts such that $\Delta z_{\text{DLA}} < 0.02$. The figure shows their distribution of $\log N(H_I)$ for candidate DLAs that are found and not found in our catalog. The distribution is shown for the “statistical” and “non-statistical” samples of N12. The statistical sample consists of confident DLA candidates with sufficiently high signal to noise to be used in Noterdaeme et al. (2012) to measure the $\log N(H_I)$ distribution and the cosmological mass density of neutral gas. We see that the overlap is very good for the statistical sample with $\log N(H_I) > 20.2$. On the other hand, the overlap for the non-statistical sample is good only for $\log N(H_I) > 20.6$.

Figure 14 shows the same distribution for the catalog of H21 where a similar behavior is seen.

Figures 15 and 16 compare the values of $\log N(H_I)$ from N12 and H21 with our values as determined by the CNN and by our fitter. The displayed samples are restricted to absorbers in the Ly α forest in order to have values of $\log N(H_I)$ for the fitter as well. However, the trend of the difference with $\log N(H_I)$ as predicted by the CNN (the blue curves) is similar when using the full sample of matched DLAs for both N12 and H21. Agreement is found at the 0.1 level, with our values being slightly greater than those of N12 and H21 at low $N(H_I)$ and slightly less than those of N12 and H21 at high $N(H_I)$. We also note that the CNN finds values that are typically 0.1 greater than our fitter.

We make the catalog available [here](#) as a FITS file. There is a line for each detected absorber with $z_{\text{QSO}} > z_{\text{DLA}}$ and $z_{\text{DLA}} \geq 2$ in sightline with $\text{BAL_PROB} = 0$. Each of the 117,458 line contains the following information:

- `THING_ID`: the SDSS identifier as found in DR16Q
- `Z_QSO`: the quasar redshift of the sightline using the `Z_LYAWG` estimator of DR16Q
- `PLATE`: SDSS spectroscopic plate of the sightline as found in DR16Q
- `MJD`: SDSS modified Julian date of observation of the sightline as found in DR16Q
- `FIBERID`: SDSS spectroscopic fiber identification of the sightline as found in DR16Q
- `RA`: right ascension of the sightline as found in DR16Q, in degrees
- `DEC`: declination of the sightline as found in DR16Q, in degrees
- `SNR`: mean signal-to-noise ratio of the sightline
- `MEAN_FLUX`: mean forest flux in $10^{-19} \text{ W m}^{-2} \text{ nm}^{-1}$. The completeness and purity of sightlines with `MEAN_FLUX` $> 2 \times 10^{-19} \text{ W m}^{-2} \text{ nm}^{-1}$ are greater than 90% for absorbers with $20.1 \leq \log N(H_I) \leq 22$.
- `Z_CNN`: the absorber redshift as found by the CNN
- `NHL_CNN`: the logarithm of the absorber column density as found by the CNN
- `CONF_CNN`: confidence parameter of the CNN over the range (0,1). Absorber with confidence > 0.5 are considered as highly confident absorbers.
- `NHL_FIT`: the logarithm of the absorber column density as found by the Voigt-profile fitter for absorbers in the rest-frame range $1,040\text{\AA} \leq \lambda_{\text{RF}} \leq 1,216\text{\AA}$ and $\log N(H_I) < 22$. This parameter is set to -1 for absorbers that do not meet the criteria.

6. CONCLUSIONS

We presented here the production of the strong-absorber catalog in the 263,201 Ly α quasar spectra of the final SDSS-IV quasar catalog from DR16 (Lyke et al. 2020). We used the CNN pipeline from Parks et al. (2018) to identify absorbers and estimate their properties z_{DLA} and $N(H_I)$. This choice was motivated by the fact that the algorithm has been constructed for low redshift and low signal to noise BOSS/eBOSS quasar spectra.

We performed completeness and purity studies of the algorithm with synthetic spectra (Etourneau et al. 2021)

produced for the eBOSS Ly α data analysis (du Mas des Bourboux et al. 2020) that reproduce the characteristics of the data sample, in terms of redshift and signal-to-noise distribution. The comparison between finder outputs and mock inputs showed that the algorithm performs well for confident DLAs with $2.2 \leq z_{\text{DLA}} \leq 3.5$, $20.3 \leq \log N(H_I) \leq 21.5$ and confidence parameter > 0.9 with both purity and efficiency > 0.9 . Reducing the sample to bright forests only with $\overline{f_{\lambda}} > 2 \times 10^{-19} \text{ W m}^{-2} \text{ nm}^{-1}$ increases efficiency and purity to > 0.9 values for a wider parameter range, for absorbers with $\log N(H_I) \geq 20.1$.

We found a bias for $N(H_I)$ toward the lowest end because the finder detects absorbers with $\log N(H_I)$ as low as 19 but overestimates this parameter just above the threshold it has been trained with. To alleviate this issue, we fit detected strong absorptions in the rest-frame range $1,040\text{\AA} \leq \lambda_{\text{RF}} \leq 1,216\text{\AA}$ with Voigt-profiles, which returns more accurate value of $N(H_I)$ than the CNN.

The algorithm detect 117,458 strong absorbers with $\log N(H_I) > 19.7$ and 57,136 DLAs with $\log N(H_I) > 20.3$, which is the largest DLA sample to date. We provided the complete results of the finder for absorbers with $z_{\text{QSO}} > z_{\text{DLA}}$, $z_{\text{DLA}} \geq 2$ and in sightlines without BALs detected in the DR16Q such that `BAL_PROB` = 0. We also provided $N(H_I)$ information of the Voigt-profile fitting for confident absorbers in the rest-frame range $1,040\text{\AA} \leq \lambda_{\text{RF}} \leq 1,216\text{\AA}$. We compared our results to previously published catalogs from Noterdaeme et al. (2012) and Ho et al. (2020) showing consistent findings.

This comprehensive analysis will enable users of this catalog to construct their own selection criteria matching the needs of their study. In addition, it highlights the regimes where DLA finders need to be improved, in particular the low-signal-to-noise regime.

ACKNOWLEDGMENTS

S.C. thanks Xavier Prochaska for his precious help and the many discussions for using the Convolutional Neural Network. The authors thank the DESI Ly α working group for providing the software to simulate the mock spectra. S.C. was partially supported by the DOE’s Office of Advanced Scientific Computing Research and Office of High Energy Physics through the Scientific Discovery through Advanced Computing (SciDAC) program.

This work was supported by the A*MIDEX project (ANR-11-IDEX-0001-02) funded by the “Investissements d’Avenir” French Government program, managed by

the French National Research Agency (ANR), and by ANR under contracts ANR-14-ACHN-0021 and ANR-16-CE31-0021.

Funding for the Sloan Digital Sky Survey IV has been provided by the Alfred P. Sloan Foundation, the U.S. Department of Energy Office of Science, and the Participating Institutions. SDSS acknowledges support and resources from the Center for High-Performance Computing at the University of Utah. The SDSS web site is www.sdss.org. SDSS is managed by the Astrophysical Research Consortium for the Participating Institutions of the SDSS Collaboration including the Brazilian Participation Group, the Carnegie Institution for Science, Carnegie Mellon University, the Chilean Participation Group, the French Participation Group, Harvard-Smithsonian Center for Astrophysics, Instituto de Astrofísica de Canarias, The Johns Hopkins University, Kavli Institute for the Physics and Mathematics of the Universe (IPMU) / University of Tokyo, the Korean Participation Group, Lawrence Berkeley National Laboratory, Leibniz Institut für Astrophysik Potsdam (AIP), Max-Planck-Institut für Astronomie (MPIA Heidelberg), Max-Planck-Institut für Astrophysik (MPA Garching), Max-Planck-Institut für Extraterrestrische Physik (MPE), National Astronomical Observatories of China, New Mexico State University, New York Uni-

versity, University of Notre Dame, Observatório Nacional / MCTI, The Ohio State University, Pennsylvania State University, Shanghai Astronomical Observatory, United Kingdom Participation Group, Universidad Nacional Autónoma de México, University of Arizona, University of Colorado Boulder, University of Oxford, University of Portsmouth, University of Utah, University of Virginia, University of Washington, University of Wisconsin, Vanderbilt University, and Yale University.

In addition, this research relied on resources provided to the eBOSS Collaboration by the National Energy Research Scientific Computing Center (NERSC). NERSC is a U.S. Department of Energy Office of Science User Facility operated under Contract No. DE-AC02-05CH11231.

REFERENCES

- Ahumada, R., Prieto, C. A., Almeida, A., et al. 2020, *ApJS*, 249, 3, doi: [10.3847/1538-4365/ab929e](https://doi.org/10.3847/1538-4365/ab929e)
- Bautista, J. E., Busca, N. G., Guy, J., et al. 2017, *A&A*, 603, A12, doi: [10.1051/0004-6361/201730533](https://doi.org/10.1051/0004-6361/201730533)
- Bird, S., Vogelsberger, M., Haehnelt, M., et al. 2014, *MNRAS*, 445, 2313, doi: [10.1093/mnras/stu1923](https://doi.org/10.1093/mnras/stu1923)
- Blanton, M. R., Bershadsky, M. A., Abolfathi, B., et al. 2017, *AJ*, 154, 28, doi: [10.3847/1538-3881/aa7567](https://doi.org/10.3847/1538-3881/aa7567)
- Cen, R. 2012, *ApJ*, 748, 121, doi: [10.1088/0004-637X/748/2/121](https://doi.org/10.1088/0004-637X/748/2/121)
- Chabanier, S., Palanque-Delabrouille, N., Yèche, C., et al. 2019, *JCAP*, 2019, 017, doi: [10.1088/1475-7516/2019/07/017](https://doi.org/10.1088/1475-7516/2019/07/017)
- Dawson, K. S., Kneib, J.-P., Percival, W. J., et al. 2016, *AJ*, 151, 44, doi: [10.3847/0004-6256/151/2/44](https://doi.org/10.3847/0004-6256/151/2/44)
- du Mas des Bourboux, H., Rich, J., Font-Ribera, A., et al. 2020, *ApJ*, 901, 153, doi: [10.3847/1538-4357/abb085](https://doi.org/10.3847/1538-4357/abb085)
- Etourneau, T., Le Goff, J.-M., Busca, N., et al. 2021, to be published in *JCAP*
- Font-Ribera, A., & Miralda-Escudé, J. 2012, *JCAP*, 2012, 028, doi: [10.1088/1475-7516/2012/07/028](https://doi.org/10.1088/1475-7516/2012/07/028)
- Fumagalli, M., Fotopoulou, S., & Thomson, L. 2020, *MNRAS*, 498, 1951, doi: [10.1093/mnras/staa2388](https://doi.org/10.1093/mnras/staa2388)
- Fumagalli, M., O’Meara, J. M., & Prochaska, J. X. 2016, *MNRAS*, 455, 4100, doi: [10.1093/mnras/stv2616](https://doi.org/10.1093/mnras/stv2616)
- Fumagalli, M., O’Meara, J. M., Prochaska, J. X., Kanekar, N., & Wolfe, A. M. 2014, *MNRAS*, 444, 1282, doi: [10.1093/mnras/stu1512](https://doi.org/10.1093/mnras/stu1512)
- Fumagalli, M., O’Meara, J. M., Prochaska, J. X., & Worseck, G. 2013, *ApJ*, 775, 78, doi: [10.1088/0004-637X/775/1/78](https://doi.org/10.1088/0004-637X/775/1/78)
- Gardner, J. P., Katz, N., Hernquist, L., & Weinberg, D. H. 1997, *ApJ*, 484, 31, doi: [10.1086/304310](https://doi.org/10.1086/304310)
- Garnett, R., Ho, S., Bird, S., & Schneider, J. 2017, *MNRAS*, 472, 1850, doi: [10.1093/mnras/stx1958](https://doi.org/10.1093/mnras/stx1958)
- Gunn, J. E., Siegmund, W. A., Mannery, E. J., et al. 2006, *AJ*, 131, 2332, doi: [10.1086/500975](https://doi.org/10.1086/500975)
- Haehnelt, M. G., Steinmetz, M., & Rauch, M. 1998, *ApJ*, 495, 647, doi: [10.1086/305323](https://doi.org/10.1086/305323)
- Ho, M.-F., Bird, S., & Garnett, R. 2020, *MNRAS*, 496, 5436, doi: [10.1093/mnras/staa1806](https://doi.org/10.1093/mnras/staa1806)
- . 2021, arXiv e-prints, arXiv:2103.10964. <https://arxiv.org/abs/2103.10964>

- Kingma, D. P., & Ba, J. 2014, Adam: A Method for Stochastic Optimization.
<https://arxiv.org/abs/1412.6980>
- Lee, K.-G., Hennawi, J. F., Spergel, D. N., et al. 2015, ApJ, 799, 196, doi: [10.1088/0004-637X/799/2/196](https://doi.org/10.1088/0004-637X/799/2/196)
- Lyke, B. W., Higley, A. N., McLane, J. N., et al. 2020, arXiv e-prints, arXiv:2007.09001.
<https://arxiv.org/abs/2007.09001>
- McDonald, P., Seljak, U., Burles, S., et al. 2006, ApJS, 163, 80, doi: [10.1086/444361](https://doi.org/10.1086/444361)
- Myers, A. D., Palanque-Delabrouille, N., Prakash, A., et al. 2015, ApJS, 221, 27, doi: [10.1088/0067-0049/221/2/27](https://doi.org/10.1088/0067-0049/221/2/27)
- Noterdaeme, P., Petitjean, P., Ledoux, C., & Srianand, R. 2009, A&A, 505, 1087, doi: [10.1051/0004-6361/200912768](https://doi.org/10.1051/0004-6361/200912768)
- Noterdaeme, P., Petitjean, P., Carithers, W. C., et al. 2012, A&A, 547, L1, doi: [10.1051/0004-6361/201220259](https://doi.org/10.1051/0004-6361/201220259)
- Ota, K., Walter, F., Ohta, K., et al. 2014, ApJ, 792, 34, doi: [10.1088/0004-637X/792/1/34](https://doi.org/10.1088/0004-637X/792/1/34)
- Palanque-Delabrouille, N., Yèche, C., Borde, A., et al. 2013, A&A, 559, A85, doi: [10.1051/0004-6361/201322130](https://doi.org/10.1051/0004-6361/201322130)
- Parks, D., Prochaska, J. X., Dong, S., & Cai, Z. 2018, MNRAS, 476, 1151, doi: [10.1093/mnras/sty196](https://doi.org/10.1093/mnras/sty196)
- Petitjean, P., Srianand, R., & Ledoux, C. 2000, A&A, 364, L26. <https://arxiv.org/abs/astro-ph/0011437>
- Pontzen, A., Governato, F., Pettini, M., et al. 2008, MNRAS, 390, 1349, doi: [10.1111/j.1365-2966.2008.13782.x](https://doi.org/10.1111/j.1365-2966.2008.13782.x)
- Prochaska, J. X., Herbert-Fort, S., & Wolfe, A. M. 2005, ApJ, 635, 123, doi: [10.1086/497287](https://doi.org/10.1086/497287)
- Prochaska, J. X., & Wolfe, A. M. 1997, ApJ, 487, 73, doi: [10.1086/304591](https://doi.org/10.1086/304591)
- . 2009, ApJ, 696, 1543, doi: [10.1088/0004-637X/696/2/1543](https://doi.org/10.1088/0004-637X/696/2/1543)
- Ross, N. P., Myers, A. D., Sheldon, E. S., et al. 2012, ApJS, 199, 3, doi: [10.1088/0067-0049/199/1/3](https://doi.org/10.1088/0067-0049/199/1/3)
- Rudie, G. C., Newman, A. B., & Murphy, M. T. 2017, ApJ, 843, 98, doi: [10.3847/1538-4357/aa74d7](https://doi.org/10.3847/1538-4357/aa74d7)
- Slosar, A., Font-Ribera, A., Pieri, M. M., et al. 2011, JCAP, 2011, 001, doi: [10.1088/1475-7516/2011/09/001](https://doi.org/10.1088/1475-7516/2011/09/001)
- Smee, S. A., Gunn, J. E., Uomoto, A., et al. 2013, AJ, 146, 32, doi: [10.1088/0004-6256/146/2/32](https://doi.org/10.1088/0004-6256/146/2/32)
- Vladilo, G., Centurión, M., Bonifacio, P., & Howk, J. C. 2001, ApJ, 557, 1007, doi: [10.1086/321650](https://doi.org/10.1086/321650)
- Wolfe, A. M., Gawiser, E., & Prochaska, J. X. 2005, ARA&A, 43, 861, doi: [10.1146/annurev.astro.42.053102.133950](https://doi.org/10.1146/annurev.astro.42.053102.133950)
- Wolfe, A. M., Turnshek, D. A., Smith, H. E., & Cohen, R. D. 1986, ApJS, 61, 249, doi: [10.1086/191114](https://doi.org/10.1086/191114)
- York, D. G., Adelman, J., Anderson, John E., J., et al. 2000, AJ, 120, 1579, doi: [10.1086/301513](https://doi.org/10.1086/301513)
- Zhu, G., & Ménard, B. 2013, ApJ, 770, 130, doi: [10.1088/0004-637X/770/2/130](https://doi.org/10.1088/0004-637X/770/2/130)